Highly coherent supercontinuum generation in a polarization-maintaining CS_2-core photonic crystal fiber

FENG XU,[1] JINHUI YUAN,[1,*] CHAO MEI,[1] BINBIN YAN,[1] XIAN ZHOU,[2] QIANG WU,[3] KUIRU WANG,[1] XINZHU SANG,[1] CHONGXIU YU,[1] AND GERALD FARRELL[4]

[1]*State Key Laboratory of Information Photonics and Optical Communications, Beijing University of Posts and Telecommunications (BUPT), Beijing 100876, P. R. China.*
[2]*Research Center for Convergence Networks and Ubiquitous Services, University of Science & Technology Beijing (USTB), Beijing 100083, P. R. China.*
[3]*Department of Physics and Electrical Engineering, Northumbria University, Newcastle upon Tyne, NE1 8ST, United Kingdom.*
[4]*Photonics Research Centre, Dublin Institute of Technology, Dublin, Ireland.*
**Corresponding author: yuanjinhui81@bupt.edu.cn*

Received XX Month XXXX; revised XX Month, XXXX; accepted XX Month XXXX; posted XX Month XXXX (Doc. ID XXXXX); published XX Month XXXX

In this paper, we design a polarization-maintaining CS_2-core photonic crystal fiber (PM-CCPCF). The two air holes at x-direction are infiltrated with C_2H_5OH in order to introduce the birefringence. By optimizing the structure parameters of the PM-CCPCF, it is demonstrated that the *x*-polarization fundamental mode has all-normal dispersion profile and the corresponding *y*-polarization fundamental mode has anomalous dispersion profile for pump wavelength 1.76 μm. Then, we investigate the supercontinuum (SC) generations when different fiber lengths, pump peak powers, and pump pulse widths are chosen, respectively. Simulation results show that for the *x*-polarization and *y*-polarization fundamental modes, highly coherent SCs can be generated by appropriately choosing the fiber length and pump pulse parameters. Finally, nonlinear propagation dynamics are analysed when the optimized fiber length and pump pulse parameters are used. The bandwidth of the SCs generated for *x*-polarization and *y*-polarization fundamental mode can be up to 0.82 and 1.26 octave, respectively. © 2018 Optical Society of America

OCIS codes: (320.6629) Supercontinuum generation; (060.5295) Photonic crystal fibers; (060.2420) Fibers, polarization-maintaining.

http://dx.doi.org/10.1364/AO.99.099999

1. INTRODUCTION

Supercontinuum (SC) generation has been attracting great research interests because of its extensive applications in wavelength-tunable light source, optical communication, optical coherence tomography [1-4]. The physical mechanism of the SC generation is resulted from a variety of nonlinear effects such as self-phase modulation (SPM), simulated Raman scatting (SRS), four-wave mixing (FWM), soliton fission (SF), etc. [1, 5-7]. The SC can be generated when pump pulse is respectively launched into the normal and anomalous dispersion regions of the nonlinear media [8, 9]. Photonic crystal fiber (PCF) is one of ideal nonlinear media for the SC generation due to its controllable group-velocity dispersion (GVD) and enhanced nonlinearity [5]. In practical applications, the bandwidth and coherence are considered as the two important performance parameters of the SC source. From the previous reports, when pump pulse works in the normal dispersion region of the PCF, the SPM and optical wave breaking dominate the nonlinear process. Although the SC generated has good coherence, its bandwidth is limited [10, 11]. In contrast, when pump pulse works in the anomalous dispersion region of the PCF, the SF is benifical to the large bandwidth, but the noise induced by the soliton dynamics will degrade the coherence of the SC [12, 13]. As the field of optical frequency metrology and synthesis develops, some works focus on obtaining the SC with high coherence in the PCFs. In 2011, Hooper *et al.* reported the SC generation in a PCF designed with all-normal GVD [14]. In 2014, Li *et al.* proposed a tapered silica PCF to achieve self-similar compression of picosecond pulse for generating the SC [15]. In 2017, Petersen *et al.* demonstrated mid-infrared SC generation in a large-mode-area chalcogenide PCF taper [16]. In 2018, Saini *et al.* investigated the coherent SC generation in chalcogenide W-type coaxial optical fiber, step-index tellurite fiber, and rib waveguide [17-19]. In the same year, Nguyen *et al.* obtained mid-infrared SC with good coherence in cascaded tellurite and chalcogenide fibers [20].

Recently, liquids including carbon disulfide (CS_2), ethanol (C_2H_5OH), carbon tetrachloride (CCl_4), and nitrobenzene ($C_6H_5NO_2$) are considered used as nonlinear materials for the SC generation [21-24]. Among these liquids, the CS_2 has large nonlinear index (about 2 orders of magnitude than silica) and broad transmission range (visible to mid-

infrared spectral region) [25-27]. Moreover, the CS_2 has reorientational nonlinearity response, which can accelerate the process of SF and improve the coherence of the SC [28, 29]. Raj *et al.* and Wang *et al.* investigated the influences of the temperature and reorientational nonlinearity response on the SC generation [30, 31]. Churin *et al.* obtained mid-infrared SC of over 600 nm in an integrated CS_2-core PCF [32]. Kedenburg *et al.* generated the SC of over 1000 nm through optimizing the dispersion profile of a CS_2-core PCF [33]. However, there is still no report on the nonlinear optical dynamics and SC generation in the CS_2-core PCF with high birefringence.

High birefringence of the PCF is usually obtained by breaking the core or cladding symmetry, which could be achieved by using the ellipse air holes or different materials to cause the refractive index difference between the two polarization directions. When input pulse is launched along the fiber polarization axis, the spectral component generated will maintain the same polarization state as input pulse [34]. Two polarization directions can provide more freedom for tailoring the dispersion and generating the SC [35]. Valliammai *et al.* obtained octave-spanning SC in a polarization-maintaining chalcogenide PCF [36]. Zhao *et al.* designed a highly nonlinear polarization-maintaining PCF and generated the SC of over 10 μm in the two polarization directions [37]. In this paper, we design a polarization-maintaining CS_2-core photonic crystal fiber (PM-CCPCF). The two air holes at *x*-direction are filled with C_2H_5OH to introduce the birefringence. When the fiber lengths, pump peak powers, and pump pulse widths are changed, the nonlinear evolutions in the process of the SC generation are numerically investigated. It is shown that highly coherent SCs can be obtained when the *x*-polarization and *y*-polarization fundamental modes of the PM-CCPCF are excited, respectively.

2. NONLINEAR THEORY MODEL

When the coupling effect between the *x*-direction and *y*-direction is neglected, the short pulse propagation in each direction of the PM-CCPCF can be respectively described by modified generalized nonlinear Schrödinger equation (GNLSE) as [5, 38]

$$\frac{\partial A}{\partial z}+\frac{\alpha_0}{2}A-\sum_{m\geq 2}\frac{i^{m+1}\beta_m(z)}{m!}\frac{\partial^m A}{\partial t^m}=i\gamma(z)\times\left(1+\tau_{shock}\frac{\partial}{\partial t}\right)\times\left[(1-f_m)|A|^2A+f_m\mu A\int_{-\infty}^{+\infty}e^{-\mu t}|A(t-t')^2|dt'\right], \quad (1)$$

where $A(z, t)$ represents the slowly varying envelope, α_0 is the linear loss of the PM-CCPCF, and $\beta_m(z)$ (m = 2, 3,..., and 12) is the m-order dispersion coefficient at propagation distance z and calculated from Taylor expansion of the propagation constant $\beta(\omega)$. The GVD parameter D is used to characteristize the dispersion. The relationship between D and β_2 can be described as

$$D=-\frac{2\pi c}{\lambda^2}\beta_2, \quad (2)$$

where c represents the light velocity in vacuum. $\gamma(z)$ is the Kerr nonlinear coefficient, which can be calculated by integration over the cross-section of the fiber as [1, 39]

$$\gamma=\frac{2\pi}{\lambda}\frac{\iint n_2(x,y)|F(x,y)|^4dxdy}{(\iint|F(x,y)|^2dxdy)^2}, \quad (3)$$

where $n_2(x,y)$ is nonlinear refractive index of CS_2 which is chosen as 2.7×10^{-18}. $F(x,y)$ represents the distribution of the electric field. Nonlinear dispersion corresponds to the effect of self-steepening (SS), which can be described as [5, 40]

$$\tau_{shock}=\frac{\gamma_1(\omega_0)}{\gamma_0(\omega_0)}=\frac{1}{\omega_0}+\frac{1}{n_2}\left(\frac{dn_2}{d\omega}\right)_{\omega=\omega_0}-\frac{1}{A_{eff}}\left(\frac{dA_{eff}}{d\omega}\right)_{\omega=\omega_0}, \quad (4)$$

where γ_1 is the derivation of γ_0 and the second and third items at the right hand represent the wavelength dependence of n_2 and effective mode area A_{eff}, respectively. The last part of Eq. (1) represents the reorientational nonlinearity [28,41]. f_m quantifies the contribution of reorientational nonlinearity among all the nonlinear effects and 6/7 is used in this work [28]. Because of large f_m, the influence of Raman scatting can be neglected. Temporal exponential decay function $\mu e^{-\mu t}$ is the response function of reorientational nonlinearity, where μ = 10 ps^{-1} is the decay rate.

The degree of coherence $g_{12}^{(1)}$ is used to characterize the quality of the SC generated [8, 40, 42]

$$g_{12}^{(1)}(\lambda,t_1-t_2)=\left|\frac{\langle A_1^*(\lambda,t_1)A_2(\lambda,t_2)\rangle}{\langle|A_1(\lambda,t_1)|^2\rangle\langle|A_2(\lambda,t_2)|^2\rangle^{1/2}}\right|, \quad (5)$$

where $A(\lambda, t)$ represents the spectrum amplitude in the frequency domain. The angular brackets represent the ensemble average over independently pairs of spectra, i.e. $A_1(\lambda, t)$ and $A_2(\lambda, t)$, which are obtained from 50 shot-to-shot simulations with different random noises at wavelength λ. We take $t_1 - t_2 = 0$ and the random noise is defined as $\sigma=\eta\overline{N}\exp(i2\pi\overline{U})$ [5, 43], where noise amplitude η is chosen as 1×10^{-3} in our simulation.

3. DESIGN OF THE PM-CCPCF

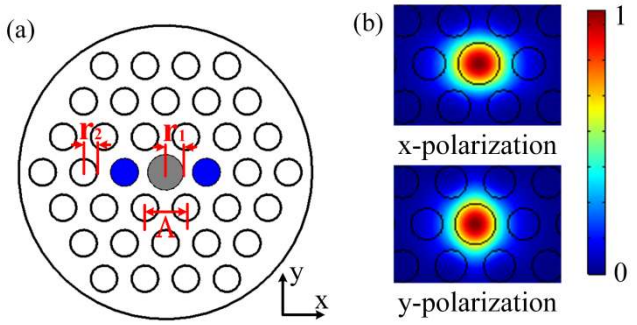

Fig. 1. (a) Cross-section of the designed PM-CCPCF. (b) The electrical field distributions of *x*-polarization and *y*-polarization fundamental modes calculated at wavelength 2.5 μm.

The cross-section of the PM-CCPCF is shown in Fig. 1(a). From Fig. 1(a), three rings of air holes are arranged with a hexagonal lattice. The Λ represents the hole-to-hole pitch, and r_1 and r_2 denote the radii of the central and cladding holes, respectively. The specific geometry parameters of the PM-CCPCF are given in Table 1. The central gray hole is infiltrated with the CS_2, whose Sellmeier equation is given as following [23, 31]

$$n_{CS_2}=1.580826+1.52389\times10^{-2}\lambda^{-2}+4.8578\times10^{-4}\lambda^{-4}-8.2863\times10^{-5}\lambda^{-6}+1.4619\times10^{-5}\lambda^{-8}. \quad (6)$$

The cladding material is the silica. To introduce asymmetry, the two air holes at *x*-direction are infiltrated with the C_2H_5OH whose linear

refractive index is given in Ref [21]. The selective-filling and sealing techniques can be used to infiltrate the liquids [44, 45]. Fig. 1(b) shows the electrical field distributions of *x*-polarization and *y*-polarization fundamental modes at wavelength 2.5 μm calculated with the full-vector finite element method. From Fig. 1(b), the two electrical field distributions clearly show the birefringence.

Table 1. Geometry Parameters of the PM-CCPCF

Geometry parameters	Λ (μm)	r_1 (μm)	r_2 (μm)
	2.15	0.9	0.7

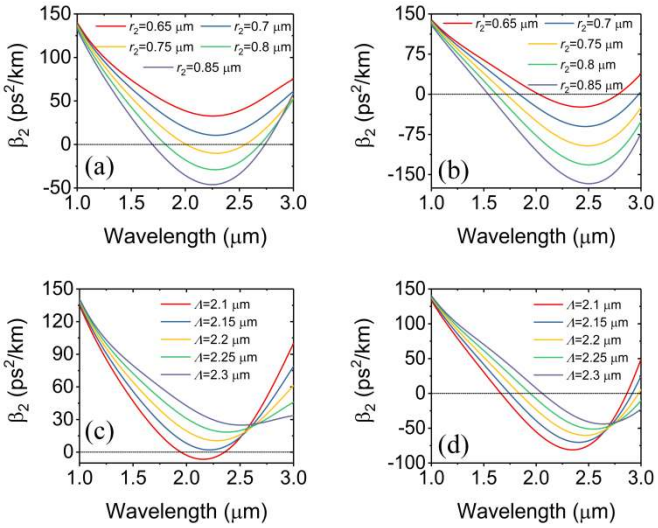

Fig. 2. β_2 of (a) *x*-polarization and (b) *y*-polarization fundamental modes of the PM-CCPCF with different r_2 when r_1 = 0.9 μm. β_2 of (c) *x*-polarization and (d) *y*-polarization fundamental modes of the PM-CCPCF with different Λ when r_1 = 0.9 μm.

By changing the structure parameters r_2 and Λ, the dispersion profiles of the PM-CCPCF can be flexibly adjusted, Figs. 2(a) and 2(b) show the β_2 curves of the fundamental modes along the *x* and *y* directions calculated as functions of r_2, respectively. With the increase of r_2, the effective refractive index difference between the core and cladding region becomes large, and the overall trending of the GVD decreases gradually, as seen from Figs. 2(a) and 2(b). When r_2 < 0.75 μm, the *x*-polarization fundamental mode shows all-normal dispersion while the *y*-polarization fundamental mode will always experience anomalous dispersion. Figs. 2(c) and 2(d) show β_2 of the *x*-polarization and *y*-polarization fundamental modes as functions of Λ, respectively. From Figs. 2(c) and 2(d), with the increase of Λ, the dispersion the value of β_2 gradually increases at the shorter wavelength and decreases at the longer wavelength. When Λ = 2.15 μm, the *x*-polarization fundamental mode appears all-normal dispersion.

We finally select r_2 = 0.7 μm and Λ = 2.15 μm, which ensure that the *x*-polarization fundamental mode keeps all-normal dispersion and *y*-polarization fundamental mode experiences a period of anomalous dispersion. Figs. 3(a) and 3(b) show the relationships between the GVD parameter *D*, γ, and wavelength. From Figs. 3(a) and 3(b), the *D* value of *x*-polarization fundamental mode is always less than 0, and the *D* value of *y*-polarization fundamental mode is larger than 0 between the two zero-dispersion wavelengths (ZDWs) of 1.75 and 2.91 μm. In addition, the effective mode areas in the two polarization axes will increase as the wavelength increases, Thus, for the *x*-polarization and *y*-polarization fundamental modes, γ reduces from 8.34 to 0.80 $W^{-1}m^{-1}$ and from 8.37 to 0.86 $W^{-1}m^{-1}$ in the wavelength range of 1.0 to 3.0 μm, respectively. To show the difference between the two polarization directions, the birefringence *B* of the PM-CCPCF is shown in Fig. 3(c), where the *B* can be up to 5 × 10^{-3} at wavelength 3 μm.

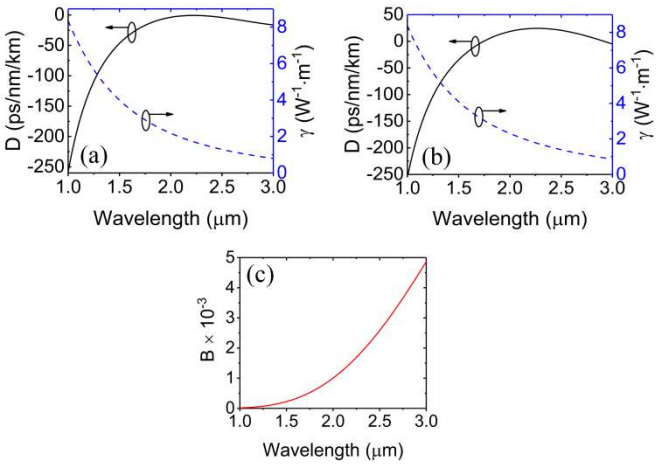

Fig. 3. The GVD parameter *D* (black solid lines) and nonlinear coefficient γ (blue dashed lines) of (a) *x*-polarization and (b) *y*-polarization fundamental modes of the PM-CCPCF. (c) The birefringence *B* of the PM-CCPCF versus wavelength.

4. SIMULATION RESULTS AND DISCUSSION

A. Influence of the PM-CCPCF length

We first investigate the influences of the fiber length on the temporal and spectral profiles and coherence when pump pulse with center wavelength 1.76 μm, width T_0 = 80 fs, and peak power P_0 = 1000 W is coupled into the *x*-polarization and *y*-polarization fundamental modes, respectively. Figs. 4(a) and 4(c) show the temporal and spectral profiles for the *x*-polarization fundamental mode, which experiences the all-normal dispersion. Because pump pulse experiences all-normal dispersion, the SPM dominates the spectral broadening. As the fiber length is increased from 3 to 9 cm with an interval of 1.5 cm, the temporal and spectral widths increase gradually, as seen from Figs. 4(a) and 4(c). The relationships between $g_{12}^{(1)}$ and wavelength with noise amplitude 1 × 10^{-3} are shown in Fig. 4(e). From Fig. 4(e), $g_{12}^{(1)}$ maintains 1 in the wavelength range considered.

Figs. 4(b) and 4(d) show the temporal and spectral profiles for the *y*-polarization fundamental mode, which experiences the anomalous dispersion under the same condition. The pump pulse is located in the anomalous dispersion region of the PM-CCPCF, so the soliton dynamics play an important role in the spectral broadening. Soliton number is defined as $N = (L_D/L_{NL})^{1/2}$, where the dispersion length L_D and nonlinear length L_{NL} are respectively defined as [5], [43]

$$L_D = \frac{T_0^2}{|\beta_2|},\ L_{NL} = \frac{1}{\gamma P_0}. \quad (7)$$

In this case, *N* is calculated as 87. Therefore, many small peaks can be observed in Fig. 4(b), corresponding to the lower-order solitons. In addition, because of the reorientational nonlinearity existing in the CS_2, solitons will occur to red-shift and separate within a short propagation distance [28]. Therefore, many solitons are separated after a 3-cm long PM-CCPCF, which extends the long wavelength sides. With the increase of the fiber length, the satellite separates to the right side and more satellites become obvious due to the SF. Moreover, because of perturbation induced by the higher-order dispersions and resonance matching condition, the blue-shifted dispersive waves (DWs) are

generated at the short wavelength sides. Fig. 4(d) shows that the spectral width can reach the maximum value covering from 1.13 to 2.71 μm when fiber length is 4.5 cm. However, with further increase of the fiber length, the spectral width keeps almost unchanged except for appearing disorder at the shorter and longer wavelength sides. Fig. 4(f) shows the relationships between $g_{12}^{(1)}$ and wavelength. From Fig. 4(f), when the fiber length is 4.5 cm, $g_{12}^{(1)}$ is almost 1 in the wavelength range considered. When fiber length is longer than 4.5 cm, many dips emerge and the coherence starts to degrade. It indicates that if we want to obtain highly coherent SC with the *y*-polarization fundamental mode, the length of the PM-CCPCF needs to be chosen appropriately.

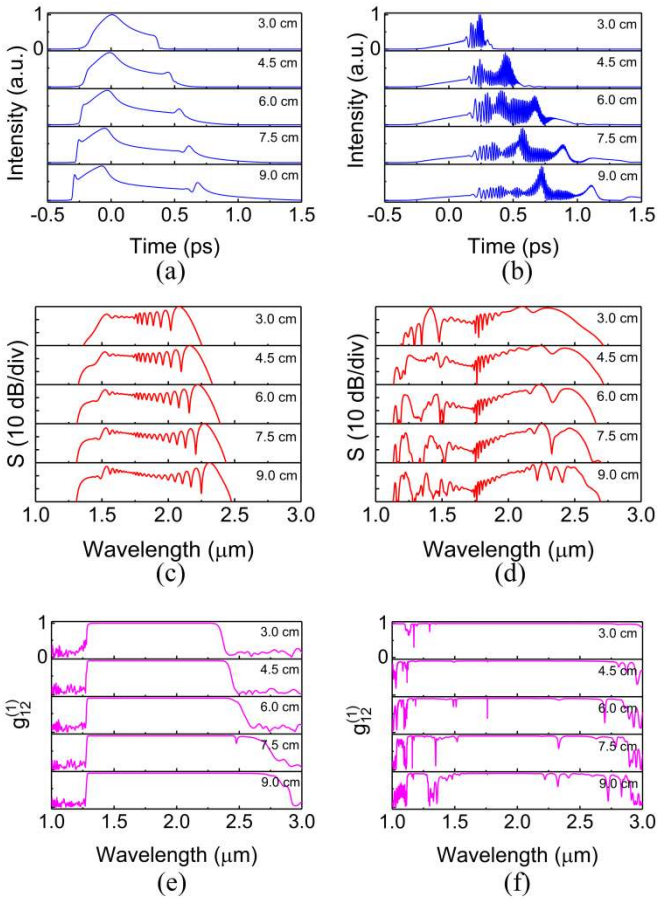

Fig. 4. (a) Temporal and (c) spectral profiles and (e) degree of coherence $g_{12}^{(1)}$ of *x*-polarization fundamental mode for different lengths of the PM-CCPCF. (b) Temporal and (d) spectral profiles and (f) $g_{12}^{(1)}$ of *y*-polarization fundamental mode for different lengths of the PM-CCPCF. *S* in (c) and (d) represents the spectrum.

B. Influence of P_0

When pump pulse with center wavelength 1.76 μm and width T_0 = 80 fs is launched into a 4.5 cm-long fiber, we investigate the influences of P_0 on the temporal and spectral profiles and coherence. Figs. 5(a) and 5(c) show the temporal and spectral profiles of the *x*-polarization fundamental mode which experiences the all-normal dispersion when P_0 increases from 500 to 3100 W. When T_0 is fixed, the spectral broadening depends on the nonlinear phase shift $\phi_{\max}$, which is defined as

$$\phi_{\max} = L_{eff} / L_{NL} = \gamma P_0 L_{eff}, \quad (8)$$

where L_{eff} represent the effective propagation distance. The spectral width is proportional to P_0. Therefore, with the increase of P_0, the spectrum becomes broader due to the SPM, and the number of oscillation peaks also increases. It is found that $g_{12}^{(1)}$ always maintains 1 when the noise amplitude is fixed at 1×10^{-3}, as seen from Fig. 5(e).

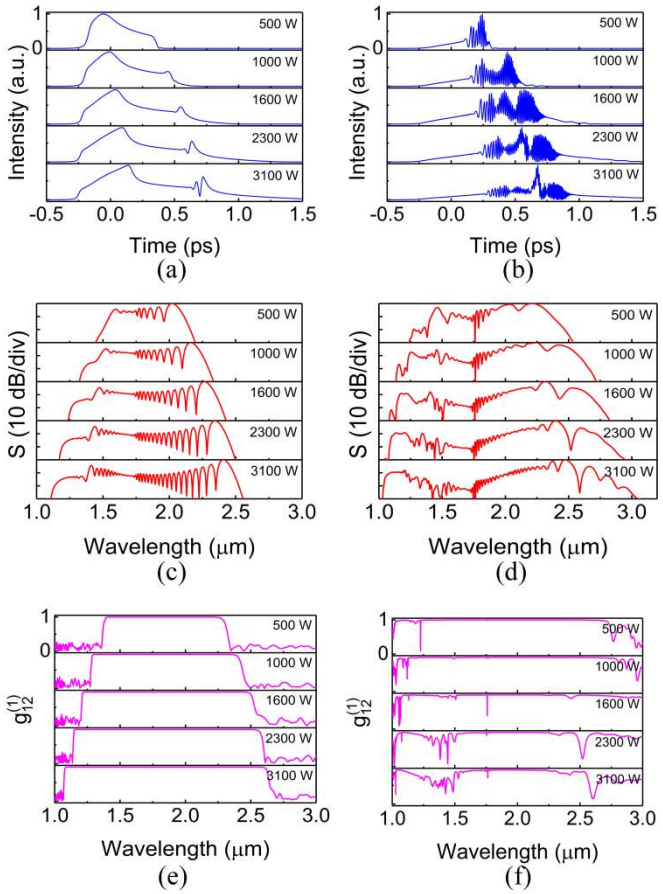

Fig. 5. (a) Temporal and (c) spectral profiles and (e) degree of coherence $g_{12}^{(1)}$ of *x*-polarization fundamental mode for P_0. (b) Temporal and (d) spectral profiles and (f) $g_{12}^{(1)}$ of *y*-polarization fundamental mode for different P_0.

The temporal and spectral profiles of the *y*-polarization fundamental mode which experiences the anomalous dispersion are shown in Figs. 5(b) and 5(d). According to Eq. (7), N = 62, 86, 110, 132, and 153 with the increase of P_0 from 500 to 3100 W. Therefore, the satellites shown in Fig. 5(b) become larger and the solitons move toward the original position at the same time. From Fig. 5(d), the spectrum gradually becomes broader as N increases. When P_0 = 3100 W, it is worth noting that when the solitons are close to the second ZDW (2.91 μm), the soliton self-frequency shift (SSFS) can be cancelled by the spectral recoil from the red-shifted DW [46, 47]. Although the spectral width is larger, the oscillation is more severe than that of lower P_0 and some dips emerge because of the degradation of the coherence with the increase of N, as shown in Figs. 5(d) and 5(f). In Ref. [5], when N < 10, the coherence is good. However, in this work, the coherence of ~1 can be obtained even if N = 62 or 87. The main reason is that the reorientational nonlinearity response of the CS_2 can effectively improve the coherence [31]. In addition, the modulation instability (MI)

length L_{MI} is calculated as ~16L_{NL}, which is equal to 1.1, 0.53, 0.33, 0.23, and 0.17 cm for different P_0, and much less than the propagation length. However, for narrow pulse of 80 fs, the influence of the MI can be significantly reduced, and good coherence can be still maintained [40, 43]. By taking the bandwidth and coherence into consideration, it is found that P_0 = 1000 W is the optimum power value.

C. Influence of T_0

Except for the fiber length and P_0, T_0 has also important influence on the temporal and spectral profiles and coherence. When P_0 is chosen as 1000 W and the fiber length is fixed at 4.5 cm, T_0 is changed from 80 to 600 fs. Figs. 6(a) and 6(c) show the temporal and spectral profiles of *x*-polarization fundamental mode which experiences the all-normal dispersion. With the increase of T_0, the temporal width becomes larger while the spectral width becomes smaller because of stronger nonlinear effect for the narrower pulse. Fig. 6(e) shows $g_{12}^{(1)}$ of the generated SC. From Fig. 6(e), $g_{12}^{(1)}$ is equal to 1 in the whole wavelength range because the SPM is the dominant effect.

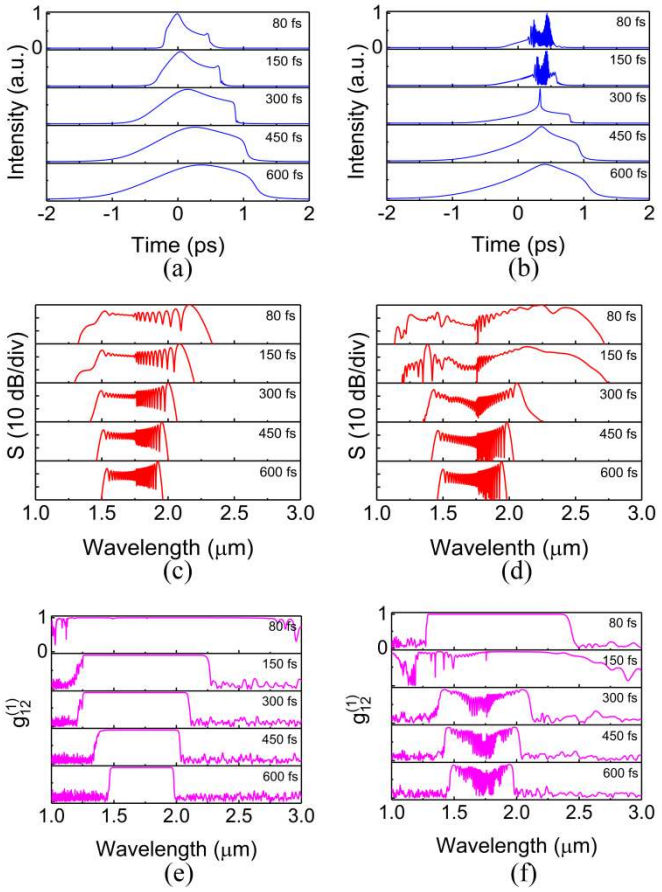

Fig. 6. (a) Temporal and (c) spectral profiles and (e) degree of coherence $g_{12}^{(1)}$ of *x*-polarization fundamental mode for different T_0. (b) Temporal and (d) spectral profiles and (f) $g_{12}^{(1)}$ of *y*-polarization fundamental mode for different T_0.

Figs. 6(b) and 6(d) show the temporal and spectral profiles of *y*-polarization fundamental mode which experiences the anomalous dispersion. N = 87, 163, 326, 489, and 652 as T_0 increases from 80 to 600 fs. When T_0 = 80 fs and 150 fs, lots of small peaks emerge in the time domain, which is caused by the SF. Correspondingly, the spectra are broadened. The soliton separation distance is proportional to T_0 [5]. Therefore, we cannot observe the apparent SF when T_0 is increased from150 to 600 fs because of the short fiber length. When T_0 > 80 fs, the coherence will be severely degraded, as shown in Fig. 6(f). The main reason is that modulation instability becomes important when T_0 is larger than 100 fs. Thus, T_0 = 80 fs is the best choice.

5. NONLINEAR PROPAGATION DYNAMICS

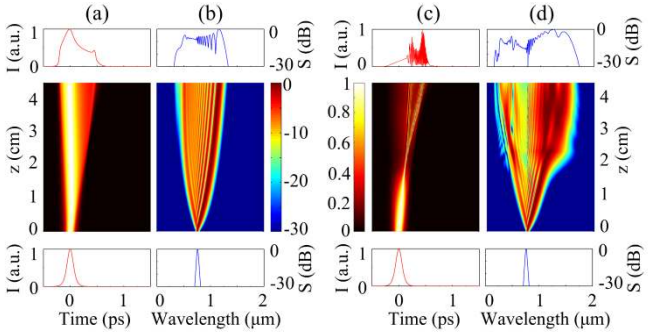

Fig. 7. For pump pulse with T_0 = 80 fs and P_0 = 1000 W, the evolutions of (a) temporal and (b) spectral profiles with *x*-polarization fundamental mode during the propagation of 4.5 cm. The evolutions of (c) temporal and (d) spectral profiles with *y*-polarization fundamental mode during the propagation of 4.5 cm. The bottom and top figures show the temporal and spectral profiles at the input and output ends of the PM-CCPCF, respectively. *I* represents the intensity.

Based on the above results, we choose the optimized pump parameters and propagation length *L*, as shown in Table 2. Figs. 7(a) and 7(b) show the temporal and spectral evolutions of *x*-polarization fundamental mode which experiences the all-normal dispersion. With the increase of the fiber length, the SPM leads to the broadening of the pulse and spectrum in the time and frequency domains. Highly coherent SC generated covers from 1.32 to 2.33 μm (0.82 octave). The severe oscillation appears at the end of the propagation.

Table 2. Optimized Pump Parameters and Characteristic Lengths

Pumping Parameters	P_0 (W)	1000
	T_0 (fs)	80
Propagation Length	L (cm)	4.5
Characteristic Lengths (*y* polarization)	L_D (cm)	2.51×10^2
	L_{NL} (cm)	3.33×10^{-2}
	L_{MI} (cm)	0.53

Figs. 7(c) and 7(d) show the temporal and spectral evolutions of *y*-polarization fundamental mode which experiences the anomalous dispersion. The soliton dynamics dominate the nonlinear evolution. The calculated characteristic lengths for *y*-polarization direction are also shown in Table 2. N = 87, which is suitable for generating a wider SC. In addition, the reorientational nonlinear response can also maintain good coherence despite large N. L_{MI} (0.53 cm) is much less than the propagation distance (4.5 cm), but the influence of MI can be efficiently reduced when narrow pulse (< 100 fs) is used. It can be seen from Figs. 7(c) and 7(d) that the solitons start to separate at z=2 cm and the spectrum is broadened quickly. However, soliton fission distance, $L_{fiss} \approx L_D/N$ [5], is calculated as 2.9 cm for *y*-polarization direction, which is longer than the numerical result. The comparison of L_{fiss} and soliton fisson distance shown in Fig. 7(c) (~2 cm) proves that the reorientational nonlinear response can accelerate the process of soliton fission. Because of the SSFS and DWs, the spectra at the short and long wavelength sides are extended with the increase of the fiber

length, and highly coherent SC is generated in the wavelength range of 1.13 to 2.71 μm (1.26 octave).

6. CONCLUSION

In summary, a PM-CCPCF is designed with the CS_2 and C_2H_5OH filled in the core and two cladding holes. The PM-CCPCF has all-normal dispersion profile for the *x*-polarization fundamental mode and anomalous dispersion profile for the *y*-polarization fundamental mode. It is shown that highly coherent SCs can be generated from 1.32 to 2.33 μm (0.82 octave) and from 1.13 to 2.71 μm (1.26 octave) when pump pulse at wavelength 1.76 μm is coupled into the *x*-polarization and *y*-polarization fundamental mode, respectively. We also investigate the nonlinear propagation dynamics when pump pulse with T_0 = 80 fs and P_0 = 1000 W and the PM-CCPCF with a length of 4.5 cm are used. It is believed that our research results can find important application in obtaining the fiber-based SC source.

Funding Information. The National Natural Science Foundation of China (61875238 and 61475023), Beijing Youth Top-notch Talent Support Program (2015000026833ZK08), Fund of State Key Laboratory of Information Photonics and Optical Communications (Beijing University of Posts and Telecommunications) P. R. China (IPOC2017ZZ05), Shenzhen Science and Technology Innovation Commission (JCYJ20160331141313917) and Research Grant Council of Hong Kong (PolyU152144/15E).

References

1. J. H. Yuan, Z. Kang, F. Li, X. T. Zhang, X. Z. Sang, Q. Wu, B. B. Yan, K. R. Wang, X. Zhou, K. P. Zhong, G. Y. Zhou, C. X. Yu, C. Lu, H. Y. Tam, and P. K. A. Wai, "Mid-infrared octave-spanning supercontinuum and frequency comb generation in a suspended germanium-membrane ridge waveguide," J. Lightwave Technol. **35**, 2994–3002 (2017).
2. H. Tu, D. L. Marks, Y. L. Koh, and S. A. Boppart, "Stabilization of continuum generation from normally dispersive nonlinear optical fibers for a tunable broad bandwidth source for optical coherence tomography," Opt. Lett. **32**, 2037–2039 (2007).
3. K. R. Tamura, H. Kubota, and M. Nakazawa, "Fundamentals of stable continuum generation at high repetition rates," J. Quantum Electron. **36**, 773–779 (2000).
4. I. Hartl, X. D. Li, C. Chudoba, R. K. Ghanta, T. H. Jo, J. G. Fujimoto, K. K. Ranka, and R. S. Windeler, "Ultrahigh resolution optical coherence tomography using continuum generation in an air-silica microstructure optical fiber," Opt. Lett. **26**, 608–610 (2001).
5. J. M. Dudley, G. Genty, and S. Coen, "Supercontinuum generation in photonic crystal fiber," Rev. Mod. Phys. **78**, 1135–1184 (2006).
6. T. North and M. Rochette, "Broadband self-pulsating fiber laser based on soliton self-frequency shift and regenerative self-phase modulation," Opt. Lett. **37**, 2799–2801 (2012).
7. M. S. Liao, X. Yan, W. Q. Gao, Z. C. Duan, G. S. Qin, T. Suzuki, and Y. Ohishi, "Five-order SRSs and supercontinuum generation from a tapered tellurite microstructured fiber with longitudinally varying dispersion," Opt. Express **19**, 15389–15396 (2011).
8. G. Genty, M. Surakka, J. Turunen, and A. T. Friberg, "Complete characterization of supercontinuum coherence," J. Opt. Soc. Am. B **28**, 2301–2309 (2011).
9. B. Kuyken, T. Ideguchi, S. Holzner, M. Yan, T. W. Hänsch, J. V. Campenhout, P. Verheyen, S. Coen, F. Leo, R. Baets, G. Roelkens, and N. Picqué, "An octave-spanning mid-infrared frequency comb generated in a silicon nanophotonic wire waveguide," Nat. Commun. **6**, 6310 (2015).
10. T. Martynkien, D. Pysz, R. Stepien, and R. Buczynski, "All-solid microstructured fiber with flat normal chromatic dispersion," Opt. Lett. **39**, 2342–2345 (2014).
11. N. R. Newbury, B. R. Washburn, K. L. Corwin, and R. S. Windeler, "Noise amplification during supercontinuum generation in microstructure fiber," Opt. Lett. **28**, 944–946 (2003).
12. X. Gu, L. Xu, M. Kimmel, E. Zeek, P. O'Shea, A. P. Shreenath, R. Trebino, and R. S. Windeler, "Frequency-resolved optical gating and single-shot spectral measurements reveal fine structure in microstructure-fiber continuum," Opt. Lett. **27**, 1174–1176 (2002).
13. N. R. Newbury, B. R. Washburn, and K. L A. Hartung, A. M. Heidt, and H. Bartelt, "Design of all-normal dispersion microstructured optical fibers for pulse-preserving supercontinuum generation," Opt. Express **19**, 7742–7749 (2011).
14. L. E. Hooper, P. J. Mosley, A. C. Muir, W. J. Wadsworth, and J. C. Knight, "Coherent supercontinuum generation in photonic crystal fiber with all-normal group velocity dispersion," Opt. Express **19**, 4902–4907 (2011).
15. F. Li, Q. Li, J. H. Yuan, and P. K. A. Wai, "Highly coherent supercontinuum generation with picosecond pulses by using self-similar compression," Opt. Express **22**, 27339–27354 (2014).
16. C. R. Petersen, R. D. Engelsholm, C. Markos, L. Brilland, C. Caillaud, J. Trolès, and O. Bang, "Increased mid-infrared supercontinuum bandwidth and average power by tapering large-mode-area chalcogenide photonic crystal fibers," Opt. Express **25**, 15336–15348 (2017)
17. T. S. Saini, N. P. T. Hoa, L. Xing, T. H. Tuan, T. Suzuki, and Y. Ohishi, "Chalcogenide W-type co-axial optical fiber for broadband highly coherent mid-IR supercontinuum generation," J. Appl. Phys. **124,** 213101 (2018).
18. T. S. Saini, T. H. Tuan, L. Xing, N. P. T. Hoa, T. Suzuki, and Y. Ohishi, "Coherent mid-infrared supercontinuum spectrum using a step-index tellurite fiber with all-normal dispersion," Appl. Phys. Express, **11**, 102501(2018).
19. T. S. Saini, N. P. T. Hoa, K. Nagasaka, X. Luo, T. H. Tuan, T. Suzuki, and Y. Ohishi, "Coherent midinfrared supercontinuum generation using a rib waveguide pumped with 200 fs laser pulses at 2.8 μm," Appl. Opt. **57**, 1689-1693 (2018).
20. H. P. T. Nguyen, K. Nagasaka, T H. Tuan, T. S. Saini, X. Luo, T. Suzuki, and Y. Ohishi, "Highly coherent supercontinuum in the mid-infrared region with cascaded tellurite and chalcogenide fibers," Appl. Opt. **57**, 6153-6163 (2018).
21. R. Raei, M. Ebnali-Heidari, and H. Saghaei, "Supercontinuum generation in organic liquid-liquid core-cladding photonic crystal fiber in visible and near-infrared regions," J. Opt. Soc. Am. B **35**, 323–330 (2018).
22. M. Vieweg, T. Gissibl, S. Pricking, B. Kuhlmey, D. Wu, B. J. Eggleton, and H. Giessen, "Ultrafast nonlinear optofluidics in selectively liquid-filled photonic crystal fibers," Opt. Express **18**, 25232–25240 (2010).
23. R. Zhang and H. Giessen, "Theoretical design of a liquid-core photonic crystal fiber for supercontinuum generation," Opt. Express **14**, 6800–6812 (2006).
24. J. Bethge, A. Husakou, F. Mitschke, F. Noack, U. Griebner, G. Steinmeyer, and J. Herrmann, "Two-octave supercontinuum generation in a water-filled photonic crystal fiber," Opt. Express **18**, 6230–6240 (2010).
25. E. K. Plyler and C. J. Humphreys, "Infrared absorption spectrum of carbon disulfide," J. Res. Natl. Bur. Stand. **39**, 59–65 (1947).
26. C. Yu, J. Liou, S. Huang, and H. Chang, "Tunable dual-core liquid-filled photonic crystal fibers for dispersion compensation," Opt. Express **16**, 4443–4451 (2008).
27. S. Yiou, P. Delaye, A. Rouvie, J. Chinaud, R. Frey, and G. Roosen, "Stimulated Raman scattering in an ethanol core microstructured optical fiber," Opt. Express **13**, 4786–4791 (2005).
28. C. Conti, M. A. Schmidt, P. S. J. Russell, and F. Biancalana, "Highly noninstantaneous solitons in liquid-core photonic crystal fibers," Phys. Rev. Lett. **105**, 263902 (2010).

29. R. Vasantha Jayakantha Raja, A. Husakou, J. Hermann, and K. Porsezian, "Supercontinuum generation in liquid-filled photonic crystal fiber with slow nonlinear response," J. Opt. Soc. Am. B **27**, 1763–1768 (2010).
30. G. Joshva Raj, R. Vasantha Jayakantha Raja, N. Nagarajan, and Ganapathy Ramanathan, "Tunable Broadband Spectrum Under the Influence of Temperature in IR Region Using CS2 Core Photonic Crystal Fiber," J. Lightwave Technol. **34**, 3503–3509 (2016).
31. L. Y. Wang, J. H. Yuan, and K. R. Wang, "Highly coherent octave-spanning supercontinuum generation in CS2-filled photonic crystal fiber with strong slow nonlinearity," Society of Photo-Optical Instrumentation Engineers. Society of Photo-Optical Instrumentation Engineers (SPIE) Conference Series, 2016:100291G.
32. D. Churin, T. N. Nguyen, K. Kieu, R. A. Norwood, and N. Peyghambarian, "Mid-IR supercontinuum generation in an integrated liquid-core optical fiber filled with CS_2," Opt. Mater. Express **3**, 1358-1364 (2013).
33. S. Kedenburg, T. Gissibl, T. Steinle, A. Steinmann, and H. Giessen, "Towards integration of a liquid-filled fiber capillary for supercontinuum generation in the 1.2–2.4 μm range," Opt. Express **23**, 8281-8289 (2015).
34. M. Lehtonen, G. Genty, H. Ludvigsen and M. Kaivola, "Supercontinuum generation in a highly birefringent microstructure fiber," Appl. Phys. Lett. **82**, 2197-2199 (2003).
35. Antoine Proulx, Jean-Michel Ménard, Nicolas Hô, Jacques M. Laniel, Réal Vallée, and Claude Paré, "Intensity and polarization dependences of the supercontinuum generation in birefringent and highly nonlinear microstructured fibers," Opt. Express **11**, 3338-3345 (2003).
36. M. Valliammai and S. Sivabalan, "Wide-band supercontinuum generation in mid-IR using polarization maintaining chalcogenide photonic quasi-crystal fiber," Appl. Opt. **56**, 4797-4806 (2017).
37. T. Zhao, Z. Lian, T. Benson, X. Wang, W. Zhang, and S. Lou, "Highlynonlinear polarization-maintaining As2Se3-based photonic quasicrystal fiber for supercontinuum generation," Opt. Mater. **73**, 343–349 (2017).
38. Y. Sato, R. Morita, and M. Yamashita, "Femtosecond optical pulse compressor using CS_2 liquid-core fiber with negative delayed nonlinear response," Jpn. J. Appl. Phys. **36**, 6768–6774 (1997).
39. D. Méchin, S. Im, V. Kruglov, and J. Harvey, "Experimental Demonstration of Self-Similar Pulse Compression and Amplification," presented at Nonlinear Guided Waves and Their Applications (NLGW), Dresden, Germany, Sep. 6–9, 2005.
40. G. P. Agrawal, "Chapter 13 supercontinuum generation," in Nonlinear Fiber Optics. Fifth ed. San Francisco, CA, USA: Academic, 2013, pp. 388–426.
41. Y. Sato, R. Morita, and M. Yamashita, "Study on ultrafast dynamic behaviors of different nonlinear refractive index components in CS2 using a femtosecond interferometer," Jpn. J. Appl. Phys., Part 1, **36**, 2109–2115 (1997).
42. J. M. Dudley and S. Coen, "Coherence properties of supercontinuum spectra generated in photonic crystal and tapered optical fibers," Opt. Lett. **27**, 1180–1182 (2002).
43. F. Xu, J. H. Yuan, C. Mei, F. Li, Z. Kang, B. B. Yan, X. Zhou, Q. Wu, K. R. Wang, X. Z. Sang, C. X. Yu, and G. Farrell, "Mid-Infrared Self-Similar Pulse Compression in a Tapered Tellurite Photonic Crystal Fiber and Its Application in Supercontinuum Generation," J. Lightwave Technol. **36**, 3514–3521 (2018).
44. Boris T. Kuhlmey, Benjamin J. Eggleton, and Darran K. C. Wu, "Fluid-Filled Solid-Core Photonic Bandgap Fibers," J. Lightwave Technol. **27**, 1617-1630 (2009).
45. R. M. Gerosa, A. Bozolan, C. J. S. de Matos, M. A. Romero and C. M. B. Cordeiro, "Novel Sealing Technique for Practical Liquid-Core Photonic Crystal Fibers," IEEE Photon, Technol, Lett,, **24**, 191-193(2012).
46. D. V. Skryabin, F. Luan, J. C. Knight, and P. St. J. Russell, "Soliton self-frequency shift cancellation in photonic crystal fibers" Science **301**, 1705–1708 (2003).
47. A. V. Gorbach and D. V. Skryabin, "Theory of radiation trapping by the accelerating solitons in optical fibers," Phys. Rev. A. **76**, 053803 (2007).